Two cascaded metasurfaces capable of generating vortex beams with distinct topological charges

XIAODONG ZHANG[a,b], JIMIN SHANG[a,b], RUILIANG ZHANG[a,b]
[a]*School of Physics and Electronic Engineering, Zhengzhou University of Light Industry, Zhengzhou 450002, China*
[b]*Henan Key Laboratory of Magnetoelectronic Information Functional Materials, Zhengzhou University of Light Industy, Zhengzhou 450002,China*

In this paper, two simple cascaded metasurfaces capable of generating vortex beams with distinct topological charges (±1, ±3) are proposed and designed. The first metasurface is a plasmonic metasurface which is composed of 21×21 elliptic nanoslits arrays perforated in an Au film. These nanoslits act as localized space-variant linear polarizers and introduce Pancharatnam−Berry phase. The second one is an all-dielectric metasurface which consists of 21×21 elliptic silicon nanopillars arrays on SiO_2 substrate. These nanopillars work as space-variant half-wave plates and result in a space-variant effective birefringence. The cascaded metasurfaces can operate at 1550 nm and the weight spectra of the desired topological charge can exceed 0.95. The cascaded metasurfaces are designed as transmission-type which makes them applied to optical fiber system. Multiple topological charges correspond to more channel capacity and different propagation directions of vortex beams are more suitable for spatial mode multiplexing. Our scheme may be a potential candidate in integrated optical communication system in future.

(Received March 1, 2021; accepted October 7, 2021)

Keywords: Plasmonic, All-dielectric, Vortex beam, Polarization

1. Introduction

Spin angular momentum (SAM), associated with circular polarization has a value of $\pm\hbar$ per photon while an optical vortex beam carries an orbital angular momentum (OAM) of $L\hbar$ per photon and has a helical phase front $\exp(iL\varphi)$. L stands for order of OAM or topological charge of photon and can take any integer value, positive or negative [1]. Due to OAM potentially has an unlimited number of states, it offers an additional freedom to increase information capacity for optical communication applications [2, 3]. Some conventional optical devices such as, cylindrical lens, spiral phase plate, spatial light modulator *et al*. can be used to generate vortex beams, but these optical elements are bulky, expensive, and not scalable to sub-wavelength size for integrated optical communication. In contrast, metasurfaces can be used for controlling the amplitude, polarization and phase of beam in sub-wavelength resolution and have some characteristics that traditional optical elements have not, such as, allowing abrupt changes of phase, eliminating the higher order diffraction and facilitating strong light-matter interaction on a sub-wavelength scale *etc*.. Meanwhile, The advanced technology and approaches on design and nanofabrications enable metasurfaces very promising available for integrated photonic chip [4].

Ebbesen group [5] discovered that the phenomenon of extraordinary optical transmission happened when light illuminated the sub-wavelength holes arrays in metal film for the first time, we called these sub-wavelength etching holes in ultrathin metal film plasmonic metasurfaces. Hasman group [6, 7] further demonstrated that light acquired an additional Pancharatnam-Berry (PB) geometrical phase by space-variant polarization manipulation. Due to Plasmonic PB-phase metasurfaces have characteristics of simple principle, easy design, broadband, indispersion *etc*., many groups trigger considerable interest into this field [8-18]. Meanwhile, all-dielectric metasurfaces have advantages of low absorption loss at optical frequencies and high transmission efficiency *etc*. that have become a hot spot [19-23]. For expanding the channel capacity of communication, we may adopt the scheme of vortex beams with more charges. However to our knowledge, many metasurfaces need to change their structures to achieve vortex beams with more charges, such as defined orientation or varying sizes of each unit. Some single metasurfaces are capable of generating vortex beams with multiple topological charges [24], but their structures are complex, and different vortex beams focus to different points that increases the design difficulty of integrated photonic devices.

This paper provides a simple and efficient approach to produce vortex beams with four distinct topological charges (L=±1, ±3) under the incident circularly polarized (CP) light by cascading a plasmonic metasurface and an all-dielectric metasurface. The first plasmonic metasurface is composed of 441 elliptic nanoslits perforated in an ultrathin Au film with 21×21 array distribution, the input light can be turned into two CP components for the

plasmonic metasurface. The second all-dielectric metasurface consists of 441 elliptic silicon nanopillars arranged into 21×21 array on SiO_2 substrate, the two CP components can be turned into vortex beams with distinct topological charges (±1, ±3) for the all-dielectric metasurface. The cascaded metasurfaces can operate at 1550 nm and has characteristics of easy fabrication, flexibility and achieving multiple topological charges that is suitable for the integrated optic communication. Thus, it provides potential for achieving vortex-beam-based photonic devices.

2. Structures

2.1. Plasmonic Metasurface Unit

The geometric parameters of elliptic nanoslit unit perforated in an ultrathin Au film are set as major radius r_1=340 nm, minor radius r_2=70 nm, thickness h=175 nm and lattice constant d=750 nm, as shown in Fig. 1a. Simply, we assume the elliptic nanoslit as a local anisotropic nanoantenna and use linearly polarized (LP) light as incident light. The numerical simulations were performed based on finite-difference time-domain (FDTD) method. Periodic boundary (Pb) conditions are applied in the x- and y-directions and perfectly matched layers (PML) conditions are applied in the z-direction. Monitors are set for obtaining the electric field of transmitted light. And, refraction index of Au has been considered for more accurate results. The wavelength ranges from 1200 nm to 2000 nm. Here, Er_1 or Er_2 denotes the transmitted electric field with the subscript r_1 (r_2) standing for the polarization of incident LP light and Er_1(r_2) shows the incident light with the linear polarization along major (minor) radius of elliptic nanoslit. Because the mediation between localized waveguide modes and surface plasmon polariton (SPP) modes contributes to intensity and polarization [25-27], we can see that Er_2 reaches almost 0.9 at 1550 nm while Er_1 is less than 0.01 over the whole band in Fig. 1b. Besides, we define extinction ratio (ER) as $10\times\log_{10}(Er_2 / Er_1)$, it can exceed 20 dB over the whole band. Thus, we can infer that the designed elliptic nanoslit can be regarded as a local linear polarizer with high performance from 1200 nm to 2000 nm and its polarization direction is along the minor radius (r_2) of nanoslit [28]. Under this circumstance, left circularly polarized (LCP) light illuminated on the single nanoslit vertically at 1550 nm. When the nanoslit was rotated from 0° to 180°, as shown in Fig. 1c, we obtained the phase of transmitted right circularly polarized (RCP) light and the relationship between the phase and the rotation angle (α) is presented in Fig. 1d. Here, it is assumed that the initial phase is zero. It is easy to find that the phase of transmitted RCP component is twice over the rotation angle of the nanoslit approximately. We can know that the additional phase results from the geometrical Pancharatnam–Berry (PB) phase of space-variant polarization manipulation from the literatures [29].

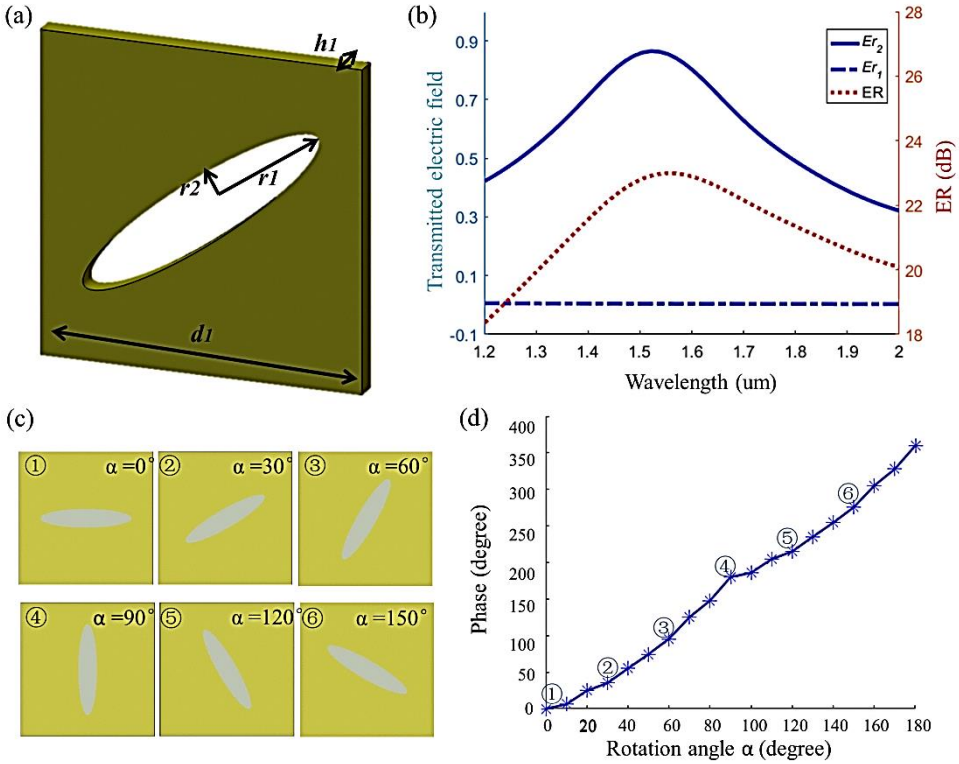

Fig. 1. (a) Dimensions of elliptic nanoslit: r1=340 nm, r2=70 nm, h_1=175 nm, d_1=750 nm. (b) The normalized transmitted electric field (Er_1 and Er_2) and the extinction ratio (ER) as a function of input wavelength (1.2-2.0 μm) for the single nanoslit unit. (c) Top views of the nanoslits with different rotation angles. (d) Relationship between the phase of transmitted RCP component and the rotation angle (α) of nanoslit under the incident LCP light at 1550 nm (color online)

Here, we arranged some elliptic nanoslits into array distribution, and every nanoslit runs in the azimuthal direction, the rotation angle (α_r) and the azimuthal angle (φ) of nanoslit satisfies the relation of, $\alpha_r=\varphi+90°$, as shown in the left of Fig. 2a. Here, additional 90° of the relation denotes these nanoslits in x axis are arranged vertically rather than horizontally. When LCP light was incident on this array vertically at 1550 nm, the transmitted RCP component became vortex beam with topological charge (+2) that our previous research had proved [30]. The far-field intensity of RCP component as function of refraction angle (θ_t) is shown in the left of Fig. 2b and the inset shows the transmitted direction of RCP component. Note that the RCP component of transmitted beam kept the same direction as LCP component, however the superposition state is not used for spatial mode multiplexing. In order to improve mode multiplexing, we designed the gradient−rotation array as a superposition of the rotation array and the gradient array [31, 32]. The unit cell of the gradient array comprises six nanoslits, it repeats with a periodicity of 4.2 μm in the x direction and the rotation angle difference is set to α_g=30° between neighbor nanoslits, as shown in the middle of Fig. 2a. As the generalized Snell's law[32] can be expressed as

$$n_t \sin\theta_t - n_i \sin\theta_i = \sigma \frac{\lambda_0}{2\pi} \frac{d\Phi}{dx} \tag{1}$$

The phase shift of transmitted RCP component equals pi/3 for normal incidence and n_i=n_t=1 from Fig. 1d. Thus the transmitted RCP component transmitted at anomalous refraction angle $\theta_t\approx20°$ while the transmitted LCP component transmitted at normal refraction angle θ_t=0° according to equation (1), as shown in the middle of Fig. 2b. So we set the rotation angle of gradient-rotation array to be $\alpha=\alpha_g+\alpha_r$, as shown in the left of Fig. 2a, the far-field transmitted intensity and transmitted direction of RCP component are shown in the left of Fig. 2b. We can see clearly that the simulated refraction direction of RCP component agree well with the generalized Snell's law and RCP component separates from the LCP component.

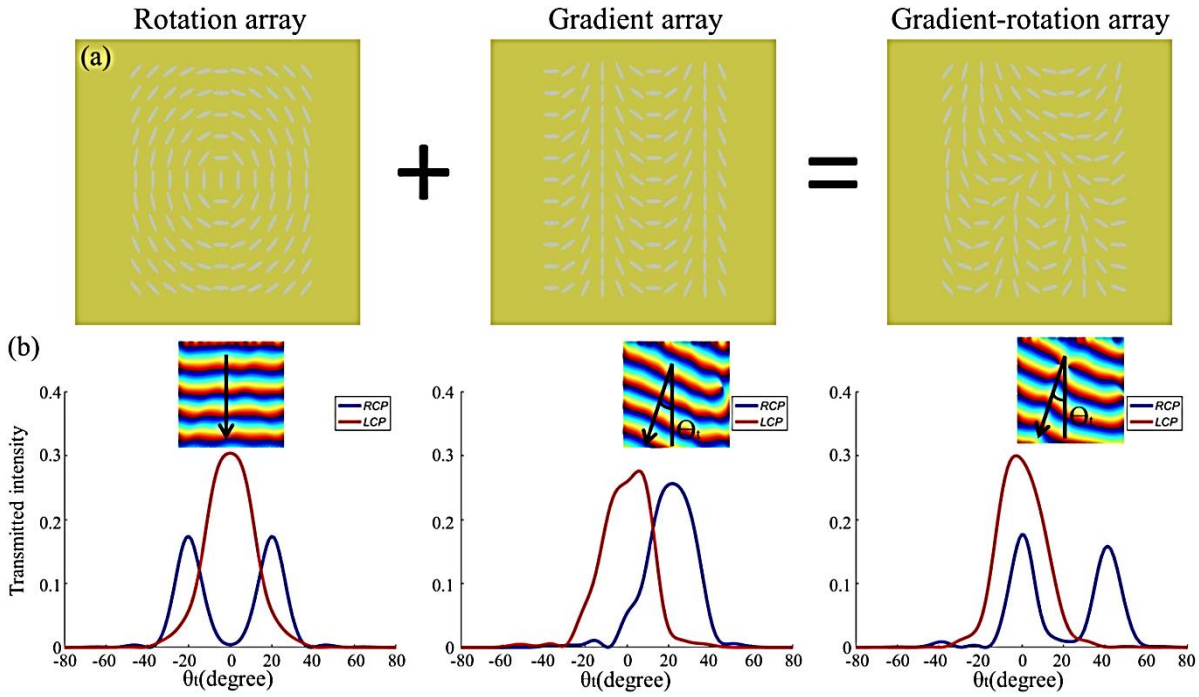

Fig. 2. (a) Three array distributions: rotation array (left), gradient array (middle), gradient−rotation array (right). (b) Far-field transmitted intensity of RCP component as a function of refraction angle (θ_t) for the corresponding arrays respectively under the incidence of LCP light at 1550 nm. Insets in (b) show the corresponding transmitted direction of RCP component (color online)

2.2. All-Dielectric Metasurface

The elliptic silicon nanopillars on SiO_2 substrate is designed as a half-wave plate with minor radius r_3 = 100 nm, major radius r_4 = 200 nm, and height h_2 = 1.8 μm. The lattice constant is d_2 = 800 nm and the thickness of substrate is h_3 = 1 μm, as shown in Fig. 3a and 3b The elliptic silicon nanopillar can be regarded as a Fabry–Pérot resonator, the effective refractive indices of the waveguide modes seriously rely on the cross section of the nanopillar. So, the ellipticity of the nanopillar leads to different transmission coefficients for incident LP light oriented along the major and minor axis of the nanopillar respectively. The simulation is also based on FDTD

method in the same conditions, the refractive index of Si and SiO_2 has been considered for more accurate results and the wavelength ranges from 1.5 μm to 1.58 μm. Here, Er_3 (r_4) denotes the normalized electric field of transmitted light with the subscript r_3 (r_4) standing for the polarization of incident LP light. It is easily found that they both keep high values as close as 1 over the whole band and the phase shifts between Er_3 and Er_4 depend on the incident wavelengths from Fig. 3c. We can see that the phase shift ($\Delta\varphi$) gets to π at 1550 nm that implies the designed elliptic nanopillar can be regarded as a half-wave plate with high performance.

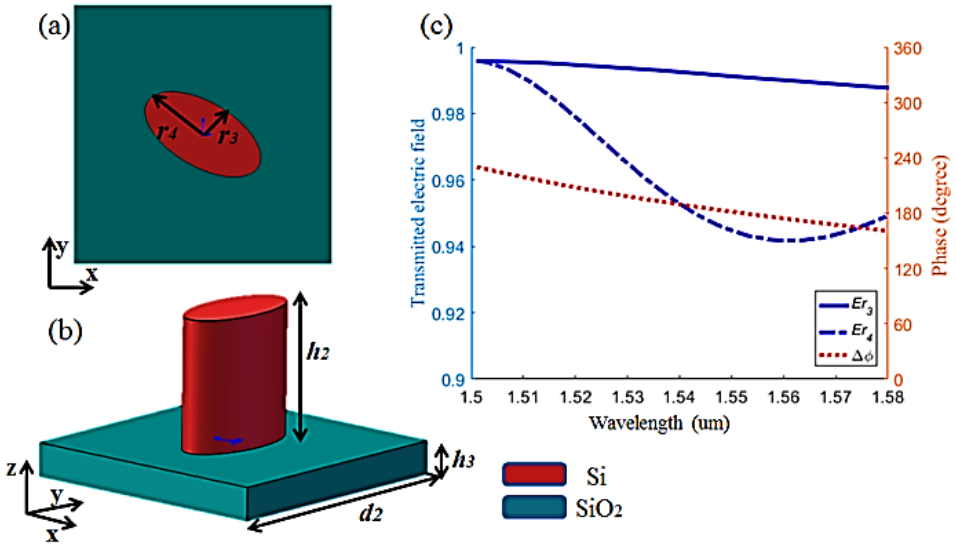

Fig. 3. (a) Top views of the elliptic nanopillar and (b) dimensions of elliptic nanopillar: r3=100 nm, r4=200 nm, h2=1.8 μm, h3=1 μm, d_2=800 nm. (c)The normalized electric field (Er_3 and Er_4) and the phase shift ($\Delta\varphi$) dependence on input wavelengths for the single nanopillar unit (color online)

3. Method

Here, we put these two metasurfaces in parallel just like the two opposite sides of a cuboid and set the distant between them to L (L=5 μm), as shown in Fig. 4. The rotation angle and the azimuthal angle of every nanoslit (nanopillar) are defined as α and φ. The first plasmonic metasurface has a size of 16×16 μm and a thickness of 175 nm. It is composed of 441 elliptic nanoslits distributed by 21×21 array with the relation of α=90°+φ. The other all-dielectric metasurface has a size of 17×17 μm and a substrate's thickness of 1.0 μm. There are 441 elliptic nanopillars arranged into 21×21 arrays on SiO_2 substrate with the relation of α=0.5×φ+90°.

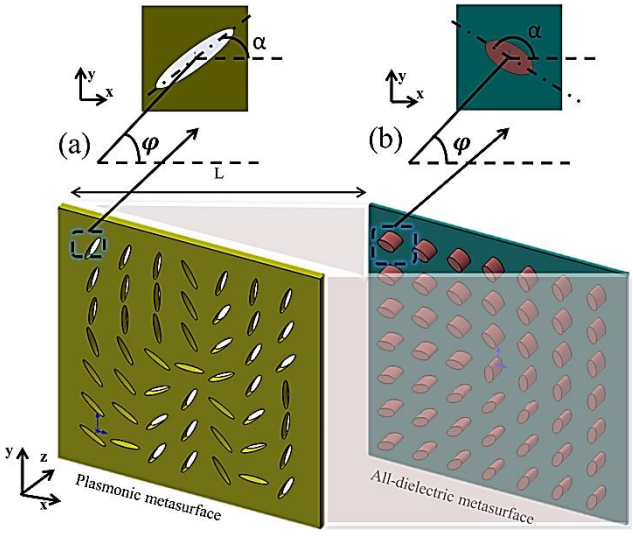

Fig. 4. Schematic structure of the designed cascading metasurfaces. (a) Geometric parameters of plasmonic metasurface: 16×16×0.175 μm, 441 elliptic nanoslits perforated in Au film and arranged by 21×21 array. (b) Geometric parameters of all-dielectric metasurface: 17×17×1.0 μm, 441 elliptic silicon nanopillars arranged into 21×21 array on SiO_2 substrate. The distance between plasmonic metasurfaces and all-dielectric metasurface is L. Inset shows rotation angle (α) and azimuth angle (φ) of nanoslit and nanopillar respectively (color online)

Next, CP light was incident on the plasmonic metasurface vertically, as depicted in Fig. 4c. Because the plasmonic metasurface is designed as transmission-type, it can be characterized by their transmission. For convenience, we adopt the Dirac bra-ket notation and denote LCP and RCP lights as $|L\rangle=\begin{pmatrix}0\\1\end{pmatrix}$ and $|R\rangle=\begin{pmatrix}1\\0\end{pmatrix}$ respectively. The action of nanoslits in the Jones calculus, neglecting absorption and reflection, can be simplified to $T_m=\mathrm{U}^{-1}\mathrm{M}^{-1}(\alpha)TM(\alpha)U$ in the helicity base, $M(\alpha)=\begin{pmatrix}\cos\alpha & \sin\alpha\\ -\sin\alpha & \cos\alpha\end{pmatrix}$ is a two-dimensional rotation matrix, $U=\frac{1}{\sqrt{2}}\begin{pmatrix}1 & 1\\ -i & i\end{pmatrix}$ is a unitary conversion matrix, $T=\begin{pmatrix}0 & 0\\ 0 & a\end{pmatrix}$ stands for a linear polarizer with polarization direction parallel to the minor axis and 'a' denotes the transmission coefficient. Thus ignoring the constant phase, the transmitted field is expressed as:

$$\left|E_m^L\right\rangle=T_m|L\rangle=\frac{a}{2}(|L\rangle+e^{+2i\varphi}|R\rangle)\ , \tag{2}$$

$$\left|E_m^R\right\rangle=T_m|R\rangle=\frac{a}{2}(|R\rangle+e^{-2i\varphi}|L\rangle)\ . \tag{3}$$

As can be seen from equations (2) and (3), when the incident CP light illuminates on the plasmonic metasurface, the transmitted light turns into two components, one is the cross-polarized component which acquires a geometric phase of $2\sigma\varphi$ and became vortex beam with topological charge (±2), and the other is the original component which does not acquire this additional phase. Meanwhile the cross-polarized component transmits at anomalous refraction angle θ_t while the original component keeps the same propagation direction as the incident light due to the role of gradient array, as depicted in the right of Fig. 2b.

In order to improve conversion efficiency of vortex beam, we used the transmitted RCP and LCP components to illuminate the all-dielectric metasurface again. Here, elliptic nanopillars of all-dielectric metasurface act as space-variant perfect half-wave plates. Then, Jones matrix of all-dielectric metasurface in the helicity base is $J_d=U^{-1}\mathrm{M}^{-1}(\alpha)JM(\alpha)U$ [33], where $J=\begin{pmatrix}1 & 0\\ 0 & -1\end{pmatrix}$ represents Jones expression of half wave plate with the fast axis along the major axis. The resulting field is:

$$E_L=J_d\left|E_m^L\right\rangle=\frac{a}{2}(e^{+i\varphi}|L\rangle+e^{+3i\varphi}|R\rangle)\ , \tag{4}$$

$$E_R=J_d\left|E_m^R\right\rangle=\frac{a}{2}(e^{-i\varphi}|R\rangle+e^{-3i\varphi}|L\rangle)\ . \tag{5}$$

From equations (4) and (5), we can know that the resulting light still be composed of RCP and LCP components, but they all acquire additionnal phases and become vortex beams, the cross-polarized component acquires a phase of $3\sigma\varphi$ and the co-polarized component acquires a phase of $\sigma\varphi$, the sign of σ depends on the handedness of incident CP light. So vortex beams with multiple topological charges (L=±3, ±1) can be achieved by cascading the two designed metasurfaces, furthermore, they can separate from each other that are suitable for mode multiplexing in integrated optical communication.

4. Simulation discussion

4.1. Intensity and phase

The simulations were performed based on FDTD method for validating the designed metasurfaces' performance. The CP light was incident vertically on the metasurfaces as excitation source and the wavelength was set to 1550 nm. PML conditions were applied in the xyz-direction, refraction index of Au, Si and SiO_2 were considered for more accurate results. The far-field intensity of transmitted light is plotted as a function of refraction angles and spatial intensity and phase pattern of RCP and LCP components are depicted in Figs. 5 and 6.

Obviously, RCP component transmits at refraction angle ($\theta_t\approx20°$) while LCP component keep the same propagation direction as the incident light under the incidence of LCP light at 1550 nm from Fig. 5. It owes to the role of gradient array. Moreover, from insets in Fig. 5a, we can also see clearly that the transmitted RCP component has features of vortex beam while LCP component has not for the plasmonic metasurface, such as helical phase pattern, concentric rings with a hollow center in the intensity profile at the beam axis, the ring radius increasing as topological charge, *etc*. The concentric rings in the intensity profile result from the geometrically propagating wave carrying the geometrical phase and the diverging wave diffracted from the singularity. The interference of the two contributions then leads to the ring effect [34]. We can judge that the topological charge of RCP component is +2 according to phase pattern and equation (2). The converted RCP and LCP components were still incident on the all-dielectric metasurface, from insets in Fig. 5 b, we can see that RCP component turns into vortex beam with topological charges (+3) while LCP component turns into vortex beam with topological charges (+1) according to phase patterns and equation (4). It is the result of spin-orbit interaction in inhomogeneous anisotropic structures [35]. Above simulation results agree well with the prediction of equation (1)-(5). It shows the designed cascaded metasurfaces are capable of generating vortex beams with distinct topological charge (+3, +1).

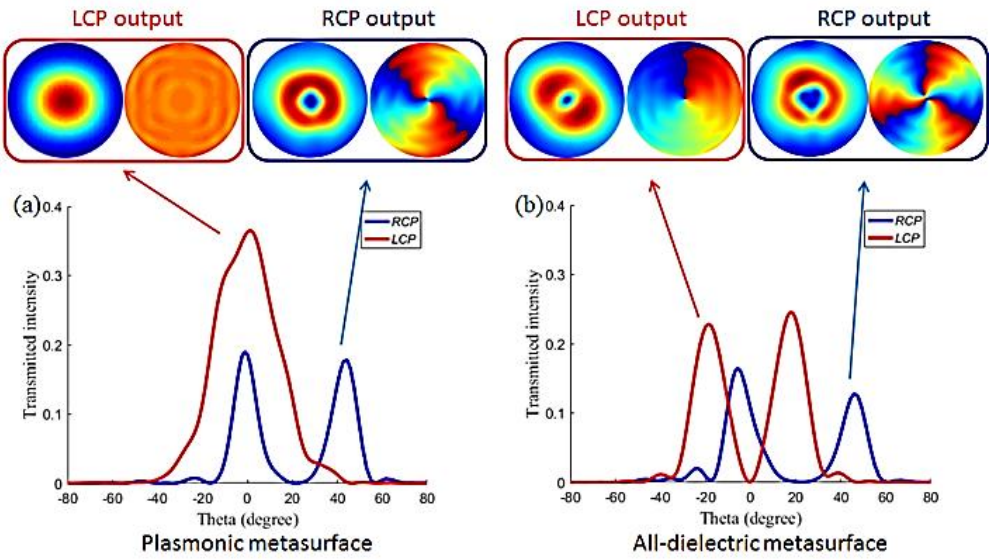

Fig. 5. The far-field transmitted intensity of RCP and LCP components as a function of refraction angle (θ) for (a) the plasmonic metasruface and (b) the all-dielectric metasurface under the incidence of LCP light at λ=1550 nm. Insets in (a) and (b) show intensity (left) and phase (right) patterns of the corresponding RCP and LCP components (color online)

Parallel results, from Fig. 6, we can see clearly that LCP component transmits at anomalous refraction angle (θ_t≈-20°) while RCP component keep the same propagation direction as the incident light under the incidence of RCP light at 1550 nm. The negative refraction angle can be explained by equation (1). According to phase patterns and equations (3) and (5), LCP component turns into vortex beam topological charges (-2) while RCP component does not for the plasmonic metasurface. Meanwhile, LCP component turns into vortex beam with topological charges (-3) and RCP component turns into vortex beam with topological charges (-1) for all-dielectric metasurface. Comparing Fig. 5 with Fig. 6, it is clear that the rotations of helical petals always keep reversed for the corresponding phase pictures. This means that their topological charges are opposite. Above simulation results also are consistent with the equations (2)-(5). Consequently it also shows the designed cascaded metasurfaces are capable of generating vortex beams with distinct topological charge (-3, -1).

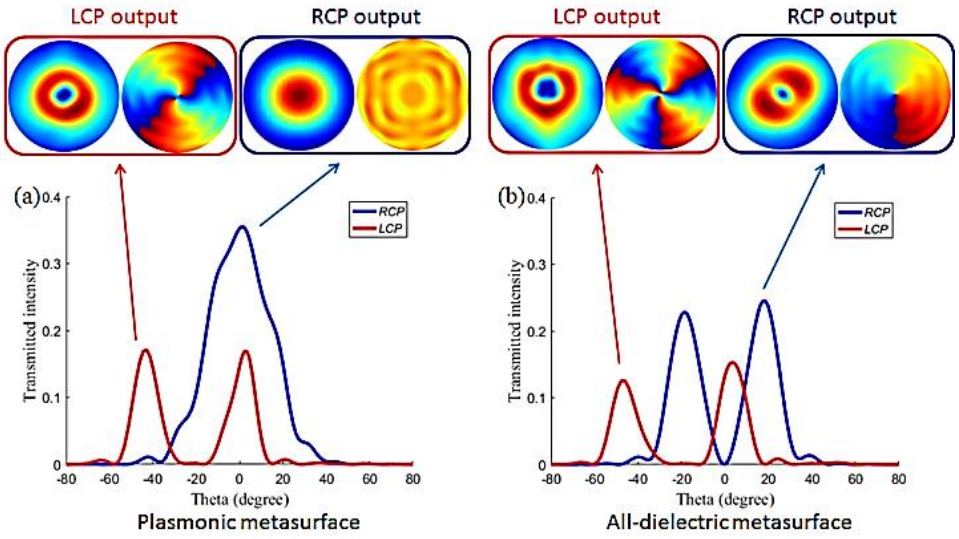

Fig. 6. The far-field transmitted intensity of RCP and LCP components as a function of refraction angle (θ) for (a) the plasmonic metasruface and (b) the all-dielectric metasurface under the incidence of RCP light at λ=1550 nm. Insets in (a) and (b) show intensity (left) and phase (right) patterns of the corresponding RCP and LCP components (color online)

It is obvious that vortex beams with multiple topological charges (±1, ±3) can be generated by cascading the designed plasmonic and all-dielectric metasurface under the incident CP light by above results, this may further increase channel capacity in optical communication. Moreover, the separation of two transmitted components makes it suitable for spatial mode multiplexing.

4.2. Fabrication tolerance

Next, we further considered the fabrication tolerance of the two metasurfaces by the performance dependence on their dimensions. We used LCP light as incident light at 1550 nm. We measured Er_1, Er_2 and ER defined as $10log_{10}(Er_2/Er_1)$ for the plasmonic metasurface when major radius of nanoslit ranged from 330 to 350 nm and minor radius of that ranged from 65 to 75 nm, the results are depicted in Fig. 7a. We can see clearly that Er_2 is much larger than Er_1 and ER >20 as the major and minor radius change, this suggests that these nanoslits can be spatial linear polarizer with high performance under the offset of their dimensions. Similarly we measured Er_3, Er_4 and their phase shift ($\Delta\varphi$) when major radius of nanopillar ranged from 195 to 205 nm and minor radius of that ranged from 97 to103 nm, the results are also depicted in Fig. 7b. we can see that Er_3>0.92, Er_4>0.95 and $\Delta\varphi$ is almost around 170°~190°, this suggests these nanopillars can also be regarded as half-wave plates under the offset of their dimensions. Meanwhile, the changes in the radius of the nanopillars are smaller than those of the nanoslits because nanopillars work based on resonators and phase shifts are more sensitive to dimensional changes. The above results indicate favorable fabrication tolerance of our design.

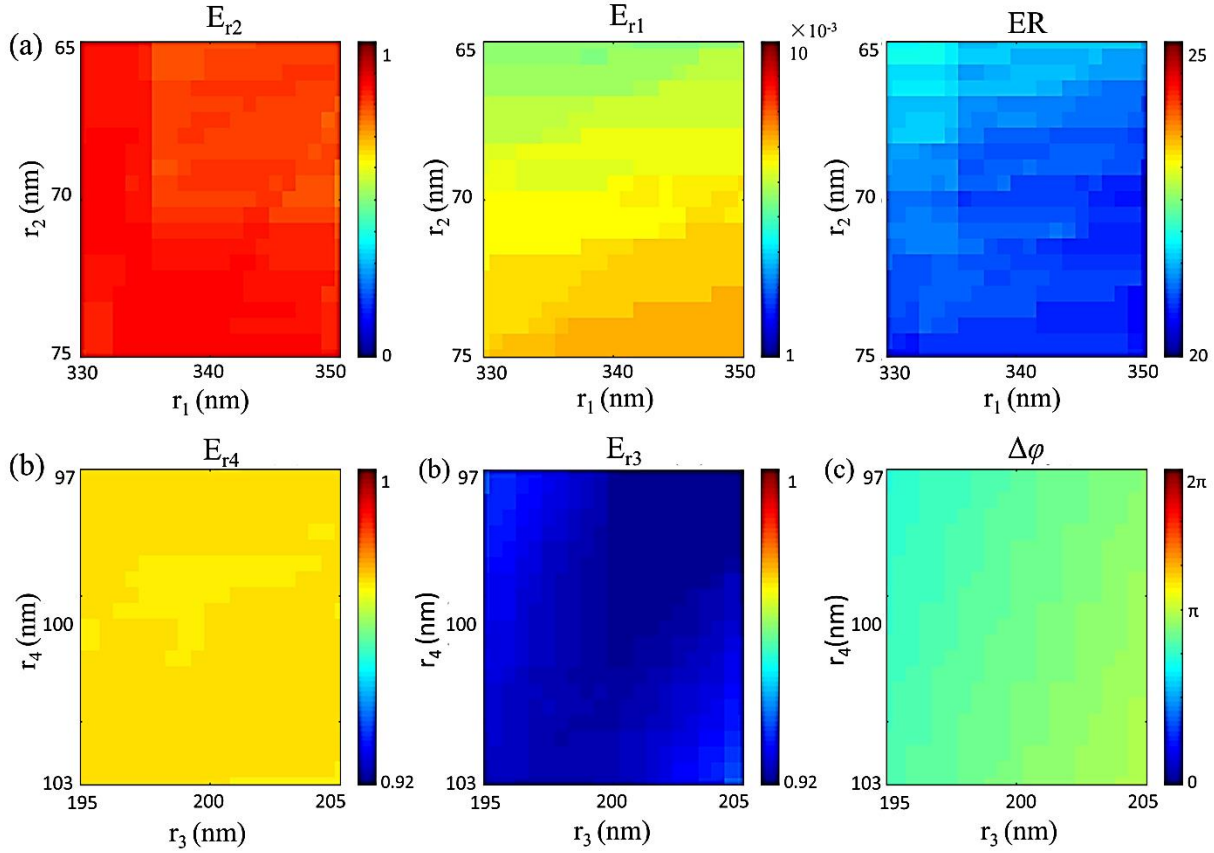

Fig. 7. (a) The dependence of Er_1 , Er_2 and ER on the major and minor radius of nanoslit and (b) the dependence of Er_3 , Er_4 and phase shift on the major and minor radius of nanopillar under the incident LCP light at 1550 nm (color online)

4.3. Weight spectra

Moreover, we calculated the weight spectra of desired topological charge, we still used LCP light as incident light at 1550 nm. Vortex field distribution $E(x, y, z)$ obtained by simulation can be projected into the spiral harmonics $\exp(in\varphi)$ [36, 37], where, n is topological charge, φ is azimuth angle. Vortex beam with spiral phase can be expressed as follow

$$E(\rho,\varphi,z)=\frac{1}{\sqrt{2\pi}}\sum_{n=-\infty}^{n=\infty}a_n(\rho,z)\exp(in\varphi)\,, \tag{6}$$

where $a_n=1/(2\pi)^{1/2}\int_0^{2\pi}E(\rho,\varphi,z)\exp(-in\varphi)d\varphi$, $E(\rho,\varphi,z)$ is the complex electric field in polar coordinates. Here, we

define $C_n = \int_0^r |a_n(\rho, z)|^2 \rho d\rho$ as the weight coefficient of the n[th] topological charge and $P_n = 10 \times \log_{10}(C_n / \sum_{q=-\infty}^{\infty} C_q)$ as weight spectra of topological charge. We calculated the weight spectra of topological charge (±1, ±3) respectively according to equation (6), results are depicted in Fig. 8. Clearly, the weight spectra of topological charges (±1, ±3) are all larger than 0.95, this further validates our design.

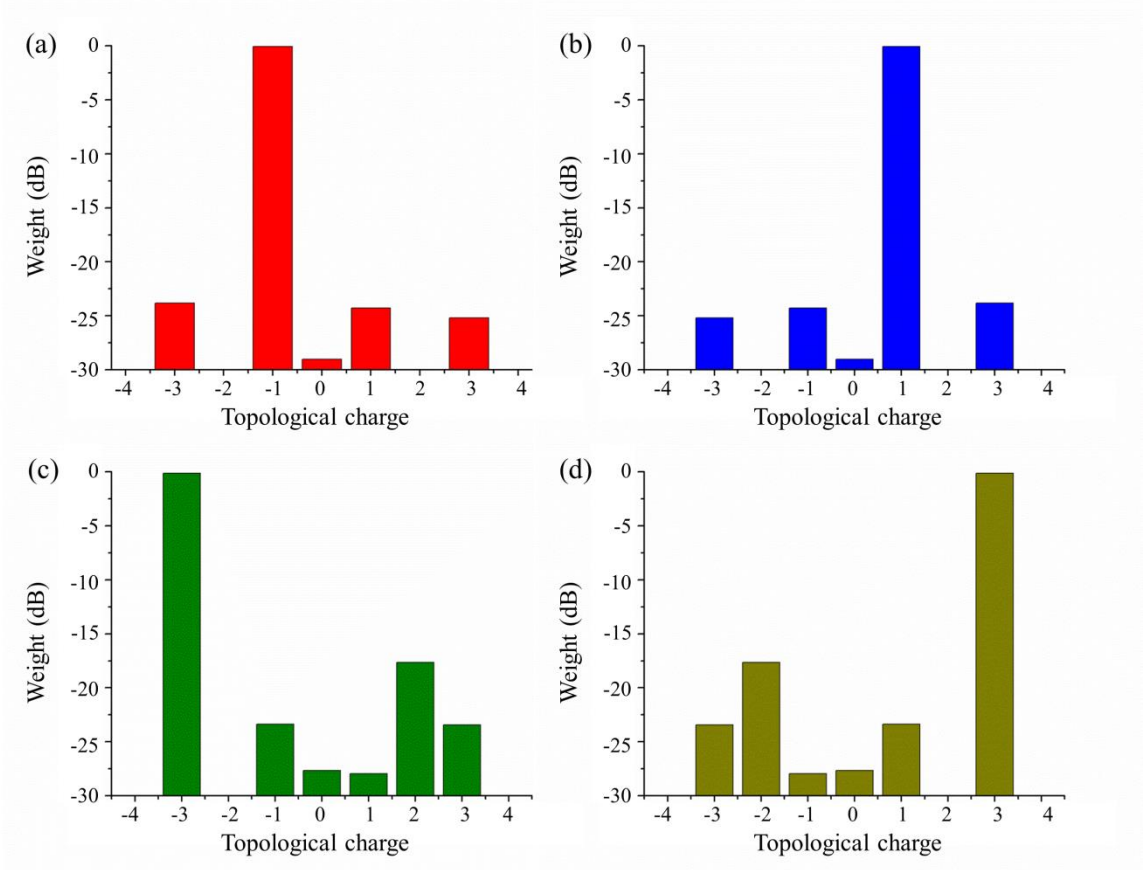

Fig. 8. Weight spectra of topological charge (a) L=-1, (b) L= +1, (c) L= -3, (d) L=+3 under the incident LCP light at 1550 nm (color online)

4.4. Flexibility

Finally, the dimension of the designed plasmonic metasurface can be scale to integrated optics. In this paper, we just show that the designed plasmonic metasurface are capable of generating vortex beam with topological charge (±2). In fact, it is capable of generating vortex beam with topological charge (±1~±4) within the same size, as shown in Fig. 9. Obviously, the four phase patterns corresponding to four array distributions shows that the topological charges of cross-polarized component is 1~4 for the plasmonic metasurface. When the cross-polarized component is illuminated on all-dielectric metasurface again, we can achieve vortex beam with topological charge (±2~±5). This suggests the flexibility of our design.

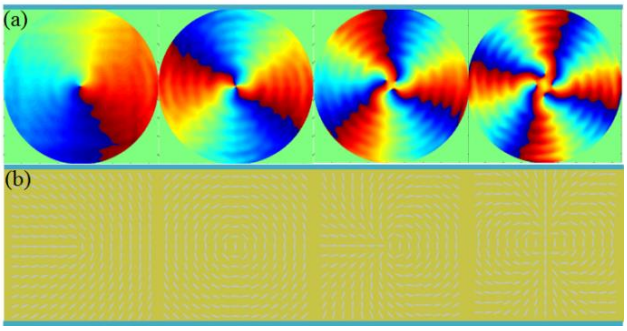

Fig. 9. (a) Four phase patterns corresponding to (b) four plasmonic metasurfaces (color online)

It should be noted that the transmission efficiency of the plasmonic metasurface is less than that of dielectric metasurfaces [38, 39]. Here, space-variant linear polarization of plasmonic metasurface causes that 50% of the power of input light can be transferred to the output

light, plus non-radiative Ohmic losses in metals *etc*. and the transmission efficiency of all-dielectric metasurface less than 1, therefore, less than 50% of the input power can be transferred to vortex beam. But the cascaded metasurfaces are designed as transmission-type which makes them easier to apply to optical fiber system. We can improve the transmittance by adjusting the structural parameters. Note that, the cascaded metasurfaces shorten the band and focus on 1550 nm, In fact we need space-variant linear polarizers to split the input light into two separated components which both turned into vortex beams with different topological charges for improving efficiency, the plasmonic metasurface has advantage of easy-fabrication, so it is easier to implement this function than other all-dielectric metasurfaces. Moreover, the bandwidth of the cascaded metrsufaces could be further expanded by optimizing all-dielectric metasurface in future.

5. Conclusions

In conclusion, we design a simple and efficient approach to generate vortex beams with distinct topological charges (±1, ±3) by cascading the plasmonic metasurface and all-dielectric metasurface under the incidence of CP light. The cascaded metasurfaces can operate at 1550 nm and the weight spectra of the desired topological charge can exceed 0.95. Simulation results agree well with theoretical derivation and validate our design. The cascaded metasurfaces have characteristics of easy fabrication, favorable fabrication tolerance and flexibility. Multiple topological charges mean different orders of OAM and bring more data transmission capacity, different propagation directions of vortex beams are suitable for spatial mode multiplexing. It should be beneficial for the development of integrated optical communication system.

Acknowledgments

This work was supported by the Natural Science Foundation of China (NSFC) [grant numbers 61905223].

References

[1] R. J. C. S. L. Allen, J. P. Woerdman, Physical Review A **45**(11), 5 (1992).
[2] E. Karimi, S. A. Schulz, I. D. Leon, H. Qassim, J. Upham, R. W. Boyd, Light Science & Applications **3**(5), 2074 (2014).
[3] C. F. Chen, C. T. Ku, Y. H. Tai, P. K. Wei, H. N. Lin, C. B. Huang, Nano Letters **15**(4), 2746 (2015).
[4] F. Monticone, A. Alù, Chinese Physics B **23**(4), 64 (2014).
[5] T. W. Ebbesen, H. J. Lezec, H. F. Ghaemi, T. Thio, P. A. Wolff, Nature **391**(6668), 667 (1998).
[6] E. Hasman, Z. E. Bomzon, A. Niv, G. Biener, V. Kleiner, Optics Communications **209**(1–3), 45 (2002).
[7] Z. Bomzon, G. Biener, V. Kleiner, E. Hasman, Optics Letters **27**(13), 1141 (2002).
[8] L. Huang, X. Chen, H. Mühlenbernd, G. Li, B. Bai, Q. Tan, G. Jin, T. Zentgraf, S. Zhang, Nano Letters **12**(11), 5750 (2012).
[9] Z. Ruan, M. Qiu, Physical Review Letters **96**(23), 233901 (2006).
[10] Z. Zhao, J. Wang, S. Li, A. E. Willner, Optics Letters **38**(6), 932 (2013).
[11] H. X. Xu, H. Liu, X. Ling, Y. Sun, F. Yuan, IEEE Transactions on Antennas & Propagation **65**(12), 7378 (2017).
[12] F. Bouchard, I. D. Leon, S. A. Schulz, J. Upham, E. Karimi, R. W. Boyd, Applied Physics Letters **105**(10), 101905 (2014).
[13] M. Kang, T. Feng, H. T. Wang, J. Li, Optics Express **20**(14), 15882 (2012).
[14] F. Ed, E. Bouchard, I. D. Leon, S. A. Schulz, J. Upham, E. Karimi, R. W. Boyd, Applied Physics Letters **105**(10), 1407 (2014).
[15] Z. Liu, Z. Li, L. Zhe, C. Hua, W. Liu, C. Tang, C. Gu, J. Li, H. T. Chen, S. Chen, ACS Photonics **4**(8), 2061 (2017).
[16] Y. Yuan, K. Zhang, B. Ratni, Q. Song, X. Ding, Q. Wu, S. N. Burokur, P. Genevet, Nature Communications **11** 1 (2020).
[17] Y. Yuan, S. Sun, Y. Chen, K. Zhang, C. Qiu, Advanced Science **7**(18), 2001437 (2020).
[18] Y. Y. Kuang Zhang, Xumin Ding,Haoyu Li, Badreddine Ratni, QunWu, Jian Liu, A. J. T. Shah Nawaz Burokur, Laser & Photonics Reviews **15**(1), 2000351 (2020).
[19] S. Jahani, Z. Jacob, Nature Nanotechnology **11**(1), 23 (2016).
[20] A. I. Kuznetsov, A. E. Miroshnichenko, M. L. Brongersma, Y. S. Kivshar, B. Luk'Yanchuk, Science **354**(6314), 2472 (2016).
[21] Y. H. Fu, A. I. Kuznetsov, A. E. Miroshnichenko, Y. F. Yu, B. Luk'Yanchuk, Nature Communications **4**(2), 1527 (2013).
[22] U. Zywietz, A. B. Evlyukhin, C. Reinhardt, B. N. Chichkov, Nature Communications **5**(s 1–4), 3402 (2014).
[23] S. Sun, Z. Zhou, C. Zhang, Y. Gao, Z. Duan, S. Xiao, Q. Song, ACS Nano **11**(5), 4445 (2017).
[24] R. C. Devlin, A. Ambrosio, D. Wintz, S. L. Oscurato, A. Y. Zhu, M. Khorasaninejad, J. Oh, P. Maddalena, F. Capasso, Optics Express **25**(1), 377 (2017).
[25] A. Degiron, T. W. Ebbesen, Journal of Optics A Pure & Applied Optics **7**(2), 5648 (2005).
[26] A. Mary, S. G. Rodrigo, L. Martínmoreno, F. J. Garcíavidal, Physical Review B Condensed. Matter. **76**(76), 195414 (2007).
[27] E. Altewischer, M. P. V. Exter, J. P. Woerdman, Journal of the Optical Society of America B **20**(9), 1927 (2002).
[28] A. Degiron, H. J. Lezec, N. Yamamoto, T. W. Ebbesen, Mineralogical Magazine **239**(1–3), 61 (2004).

[29] F. Cardano, E. Karimi, S. Slussarenko, L. Marrucci, L. C. De, E. Santamato, Applied Optics **51**(10), C1 (2012).
[30] X. Zhang, D. Kong, S. Li, L. Wang, Optik **175** 319 (2018).
[31] J. Zeng, L. Li, X. Yang, J. Gao, Nano Letters **16**(5), 3101 (2016).
[32] N. Yu, F. Capasso, Nature Materials **13**(2), 139 (2014).
[33] A. K. A. Ghatak, Polarization of light with applications in optical fibers (SPIE PRESS, 2011).
[34] W. Shu, Y. Liu, Y. Ke, X. Ling, Z. Liu, B. Huang, H. Luo, X. Yin, Optics Express **24**(18), 21177 (2016).
[35] L. Marrucci, C. Manzo, D. Paparo, Physical Review Letters **96**(16), 163905 (2006).
[36] L. Torner, J. Torres, S. Carrasco, Optics Express **13**(3), 873 (2005).
[37] N. Yu, P. Genevet, F. Aieta, M. A. Kats, R. Blanchard, G. Aoust, J. P. Tetienne, Z. Gaburro, F. Capasso, IEEE Journal of Selected Topics in Quantum Electronics **19**(3), 4700423 (2013).
[38] A. Arbabi, Y. Horie, M. Bagheri, A. Faraon, Nature Nanotechnology **10** (11), 937 (2015).
[39] R. C. Devlin, A. Ambrosio, N. A. Rubin, J. P. B. Mueller, F. Capasso, Science **358**(6365), 896 (2017).

*Corresponding author: zhangxiaodong@zzuli.edu.cn